communications physics

Article

https://doi.org/10.1038/s42005-024-01781-9

Unforeseen advantage of looser focusing in vacuum laser acceleration

Check for updates

Aitor De Andres[1,3] ✉, Shikha Bhadoria[2,3] ✉, Javier Tello Marmolejo[2], Alexander Muschet[1], Peter Fischer[1], Hamid Reza Barzegar[1], Thomas Blackburn[2], Arkady Gonoskov[2], Dag Hanstorp[2], Mattias Marklund[2] & Laszlo Veisz[1] ✉

Acceleration of electrons in vacuum directly by intense laser fields holds great promise for the generation of high-charge, ultrashort, relativistic electron bunches. While the energy gain is expected to be higher with tighter focusing, this does not account for the reduced acceleration range, which is limited by diffraction. Here, we present the results of an experimental investigation that exposed nanotips to relativistic few-cycle laser pulses. We demonstrate the vacuum laser acceleration of electron beams with 100s pC charge and 15 MeV energy. Two different focusing geometries, with normalized vector potential a_0 of 9.8 and 3.8, produced comparable overall charge and electron spectra, despite a factor of almost ten difference in peak intensity. Our results are in good agreement with 3D particle-in-cell simulations, which indicate the importance of dephasing.

Vacuum laser acceleration (VLA) is a particle acceleration paradigm where electrons gain net energy from the interaction with a laser field in vacuum. The maximum accelerating electric field in VLA, which is controlled by the laser power and focusing geometry, exceeds 1 TV/m for typical state-of-the-art multi-TW lasers. Thus, it significantly exceeds the field strength in other acceleration scenarios, such as conventional radio-frequency acceleration[1], dielectric laser acceleration[2], direct laser acceleration (DLA)[3], laser-wakefield acceleration (LWFA) or plasma-wakefield acceleration[4]. This makes VLA a promising candidate for a future electron source due to its high accelerating field (>TV/m compared to 10—few-100 GV/m in DLA and LWFA), short acceleration length (<100 μm compared to few-100 μm to many cm in DLA and LWFA) and short bunch duration (few-100 attosecond compared to few-fs to 100 fs in DLA and LWFA).

However, the interplay between the physical mechanisms that drive VLA in the relativistic regime is not fully understood. Two relevant acceleration mechanisms have been identified in simulations: capture and acceleration scenario[5,6], taking place over many Rayleigh ranges with moderate accelerating gradients, and focal spot acceleration[7], concentrated within one Rayleigh range around the focus with much stronger gradients. However, none of the theoretical models[7–13] have been experimentally verified; existing experimental works have relied on simulations to support their observations rather than in analytic theory and its derived predictions. This is due to the challenging requirements of VLA. The initial electron bunches must (1) have relativistic energy, such that they propagate with the laser for a certain distance, (2) have sub-femtosecond duration, such that they fit in the half-cycle long accelerating phase of the electromagnetic pulse, and (3) be injected into the right phase of laser field near to its spatio-temporal maximum.

The state of the art in VLA includes only few experiments, some in the ponderomotive regime, where electrons oscillate in the laser field and reach non- or slightly relativistic energies[14–17], and some in the VLA regime, where one part of the electrons interact only with one optical cycle and reach strongly relativistic energies[18–20]. A former result[21] in the ponderomotive regime is even strongly contested[22,23].

Alternatively, radially polarized laser pulses were also proposed for VLA[24,25], but only non-relativistic energies have been demonstrated[26,27]. Recent works have realized VLA with linear laser polarization up to multi-MeV energies using different objects as electron source, such as large fused silica targets[18], nanotips[19], thin foils[20], and micro-bars[17]. However, the underlying acceleration mechanism and the competing roles of electric field strength and acceleration distance have been sparsely investigated.

Here, we report the result of an experimental campaign using the sub-5-fs Light Wave Synthesizer 20[28] to drive VLA from nanotips, using two different focusing geometries, as characterized by their differing f-numbers (f#). We experimentally investigate for the first time the dependence of the VLA process on the focusing geometry and how electrons dephase in the accelerating laser field.

We show that comparable electron energies (around 15 MeV) are obtained in both loose and tight focusing despite almost an order of magnitude difference in laser intensity. We explain this in terms of the interplay between laser electric field strength and accelerating distance. We also measure a hole in the electron angular distribution, which is caused by the

[1]Department of Physics, Umeå University, Linnaeus väg 24, Umeå, 90187, Sweden. [2]Department of Physics, University of Gothenburg, Origovägen 6B, Göteborg, 41296, Sweden. [3]These authors contributed equally: Aitor De Andres, Shikha Bhadoria. ✉e-mail: aitor.de.andres@umu.se; shikha.bhadoria@mpi-hd.mpg.de; laszlo.veisz@umu.se

influence of the laser and provides further evidence that VLA is the relevant process[18,20].

Results and discussion

Experimental approach

Our experimental approach to realize VLA is to place a nanometric target, i.e., the apex of a nanotip, in the focus of a high-intensity ($I \geq 10^{18}$ W/cm^2) 4.8 fs laser pulse[29–32] (see sections Laser and Target alignment for experimental details), as demonstrated with a few-cycle laser by Cardenas[19]. This case (shown in Fig. 1a) contains two steps[33,34]. Initially, the laser ionizes the tip into a highly overdense plasma. Then, the combined laser field and the fields of the nanoplasma extract one bunch of electrons every half optical cycle, accelerating them to a relativistic initial energy at time t_1. Every second bunch propagates at an initial angle θ_1 to the laser propagation direction as approximately predicted by the Mie theory. In the second stage, the bunch undergoes vacuum laser acceleration, becoming increasingly aligned with the laser propagation direction around time t_2. Finally, the acceleration terminates when the electrons escape the region of strong fields after a distance of about one Rayleigh length, with a final angle θ_2. By using a sub-two cycle laser pulse with a certain carrier-envelope phase (CEP), we are able to generate in one of the two directions an essentially isolated electron bunch, as indicated by the numerical simulations that we later present.

Experimental results

The electron angular charge distributions are compared for an experiment with f#1 and another one with f#3 focusing in Fig. 2; for experimental details see section Electron beam characterization. Panels (a) and (b) show distributions of electrons above 130 keV with a broad range of propagation directions, with a hole in the center for f#3. We confirmed that the hole is related to the diffraction of the laser beam by halving the beam diameter with an iris, which reduced the diameter of the hole (not shown). Despite the difference in intensity, the overall average charge is comparable in both cases: 179 pC (432 pC in best case) and 265 pC (369 pC in best case) for f#1 and f#3, respectively. Inserting the lead shield (panels (c) and (d)) shows electrons above 2.5 MeV and reveals two distinct peaks, displaced from the center along the polarization direction. The average charge is decreased to 29 pC (56 pC in best case) and 5.4 pC (12.8 pC in best case) for f#1 and f#3, respectively. This angular pattern was repeatedly observed despite shot-to-shot fluctuations, especially in the polar angle (±5°), as described in section Target alignment stability. For convenience, the high-energy charge distribution has also been plotted against the azimuth angle (i.e., integrated over the polar angle) in Supplementary Fig. 3 and discussed in Supplementary discussion: Charge vs azimuth.

Due to the reduced intensity for f#3 focusing, the accelerated beams are expected to have lower total charge and lower electron energy. However, this is not the case, as visible from the angle-resolved energy spectra shown in Fig. 3a and c. For f#1, maximal energies >15 MeV were observed at 10° from the laser axis, although electrons with >5 MeV were observed across the broad range of azimuthal angles (0° to 30°). For f#3, similarly high maximal energies were observed (>15 MeV), albeit in a narrower angular range: e.g. at 0° and 20° no electrons with >5 MeV are seen. Nonetheless, despite overall similar charge, a larger number of high-energy charge is observed for f#1.

Simulations

In order to gain insights into the experimental results, we performed particle-in-cell (PIC) simulations using Smilei-v4.7[35], for the details of the simulation see section PIC Simulations. By tracking particles over a sufficiently long distance we are able to explain the high performance of f#3 focusing, as well as the angular structure of the electron beams.

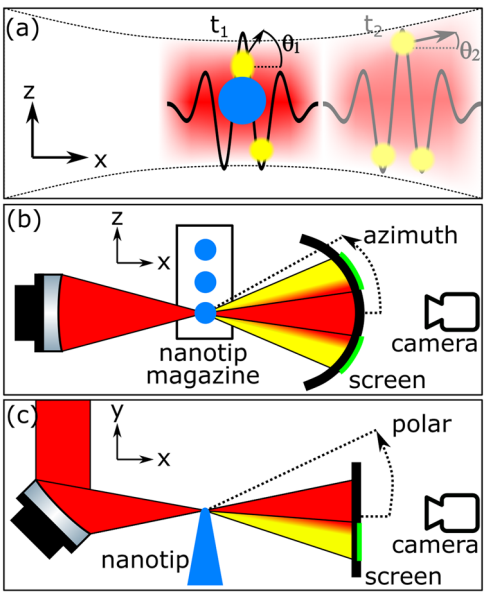

Fig. 1 | Acceleration principle and experimental setup. Acceleration mechanism in two steps: **a** electron bunches (yellow) are extracted from a nanotip (blue) at t_1 and accelerated via VLA around t_2. Experimental setup: top (**b**) and side (**c**) view. The nanotip magazine positions the tips into the laser focus (laser in red). Electrons are diagnosed by scintillating screen detectors or a spectrometer (not shown). The laser polarization direction (along z) is perpendicular to the axis of the nanotip.

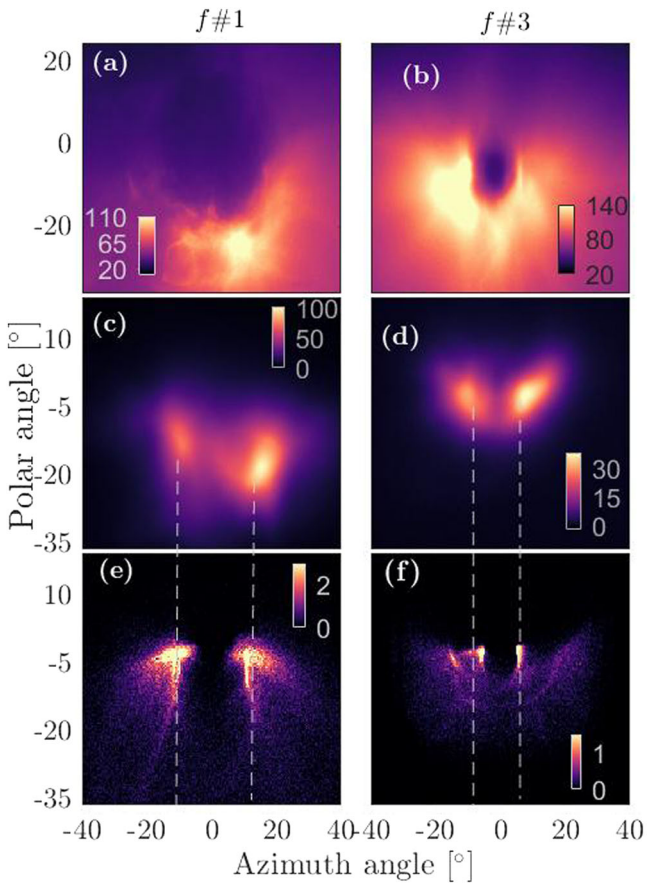

Fig. 2 | Charge distribution characterization. Angularly resolved charge distributions of electrons in units of pC/sr, for the cases of focusing by f#1 (**a**, **c**, **e**) and f#3 (**b**, **d**, **f**) optics. Electrons with measured energy above 130 keV are shown in **a**, **b**, and above 2.5 MeV in **c**, **d**. Distributions of electrons from simulation results with energies above 100 keV are shown in **e**, **f**. Experimental results [(**a**) to (**d**)] are averaged over a number of shots. Vertical dashed lines in **c** to **f** indicate the peak positions of the experimental electron distribution.

We begin by showing the spatial and angular distributions of the accelerated electrons, when they have travelled approximately one Rayleigh length from the nanotip. Figure 4a (the view in the $x-z$ plane) shows a train of electron bunches (labelled A to D) that are spaced half a wavelength apart and propagate with the laser pulse, with a deflection from the x axis that alternates from bunch to bunch. The number density of individual electron bunches in this train depends on the CEP of the laser, as previously investigated in refs. 19,34, and with a CEP of $\sim 0.3\pi$ rad, an isolated electron bunch is generated on one side. The spatial distribution in the $y-z$ plane, shown in Fig. 4b, reveals two distinct peaks outside the region of highest intensity, in locations that correspond to azimuth angles of about $\pm 13°$ and a polar angle of about $-5°$, in good agreement with the experiments. Greater detail about the simulation results can be found in Supplementary note: PIC Simulation details. The expected propagation angle for an initially resting electron in a plane wave is[36] $\theta_2 = \arctan[\sqrt{2/(\gamma-1)}]$, where γ is the Lorentz factor of the electron. This predicts azimuth angles 13-24° for electron energies of 5–18 MeV. This is also visible in Fig. 5 that plots the maximum electron energies and the corresponding calculated propagation angle of the bunches for both focusing geometries. The simulated propagation angles converge towards the theoretically predicted value by $\arctan[\sqrt{2/(\gamma-1)}]$ and are consistent with the experimental results.

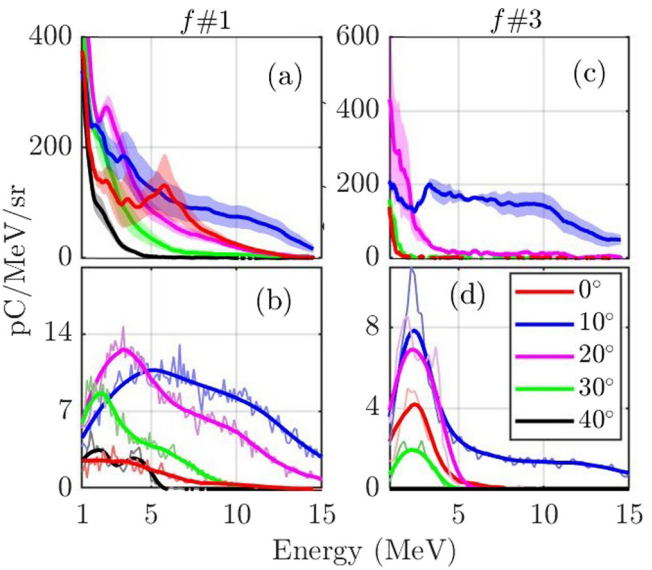

Fig. 3 | Electron energy spectra at varying propagation directions. Angle-resolved electron spectra with the f#1 (**a**, **b**) and f#3 (**c**, **d**) configuration. Panels **a**, **c** are experimental averaged electron energy spectra resolved along the azimuth angle. The shaded area in **a**, **c** represents the standard deviation over several (3–5) shots. Panels **b**, **d** are simulated angle-resolved electron spectra at certain azimuth angles. The range of angles around [0–40°] over which the electron spectra is integrated in panels **b**, **d** is chosen in accordance with the approximate width of the detector window (spectrometer acceptance angle), i.e., a polar and azimuth angle of about ± 6. 1° for f#1 and ± 4. 5° for f#3. The lighter lines in background of **b**, **d** are raw simulation data and the thick lines are their smoothed version.

The simulated and measured angular charge distributions are compared in Fig. 2. In the simulations in Fig. 2e for f#1 the presence of two distinct peaks is reproduced well (see dashed lines highlighting the agreement in the azimuth angle), and in Fig. 2f for f#3 the anticipated 'hole' in the distribution is also visible (the radius of hole agrees well with the measurements)[18,20]. We attribute the difference between measured and simulated low energy electron angular distribution (especially around zero degree) to the short, but not zero electron density preplasma scale length in the experiments (see Supplementary Fig. S4 of Cardenas[19]). The accelerated charge in the simulations (16.7 and 23.6 pC above 100 keV for f#1 and f#3, respectively) is about one order of magnitude less than in the experiments, which approximately corresponds to the ratio between experimental ($1500n_c$) and simulated ($100n_c$) electron densities in the tip. The simulated electron energy spectra, shown in Fig. 3b and d, are similar to the experimental results: the highest energies (>15 MeV) and greatest charge is found for 10°. For f#1 the distribution of these energetic electrons extends towards 20° and slightly towards 0°. Notably, for f#3 a plateau extending up to about 15 MeV is clearly seen for 10°, while almost no electrons exceed 5 MeV for other angles. A difference in the very low energy region of the tightly focused case in Fig. 3b might point to a need to model the laser or the preplasma scale length more appropriately. Nevertheless, with high energy electrons in mind, the simulations closely match the experiments. Furthermore, the charge, energy and angular distribution of individual bunches slightly depends on the CEP[19,34]. The CEP was not stabilized in the experiments, thus averaging over multiple shots is equivalent with averaging over the CEP. As the CEP was fixed in simulations, to compensate for CEP changes the spectra in two directions, corresponding to π-shifted CEP, were averaged over. We note that our modelling uses the paraxial approximation for the focusing fields[7,11]. While these limitations play a role, as indicated by the differences between results of simulations and experiments, our modelling appears to be sufficient to explain the counter-intuitive phenomena we have observed.

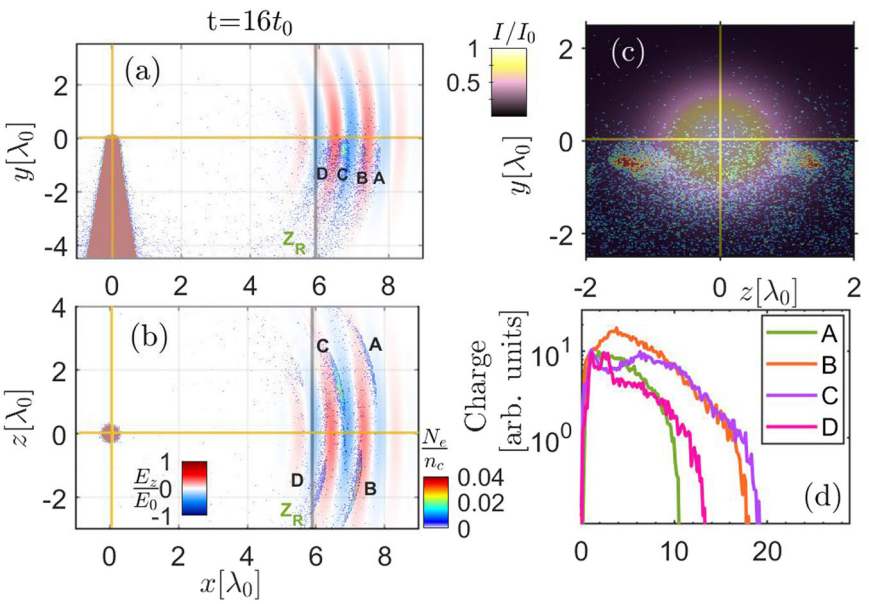

Fig. 4 | Simulated electron bunch propagation and energy spectra. Simulated electron distribution from all angles: **a** Side view of *f*#1 case, with laser electric field plotted over the electron density in (x-y) space, **b** top view of the same in (x-z) space. Each individual electron bunch is labelled from A to D and the shaded gray line marks one Rayleigh length (Z_R) from the focus at nanotip (where the solid yellow lines cross). **c** Total moving electron density in (y-z) space, plotted over the average laser intensity. **d** Energy distribution of individual electron bunches. All the panels are plotted at $16t_0$ when all electron bunches have already crossed a Rayleigh length.

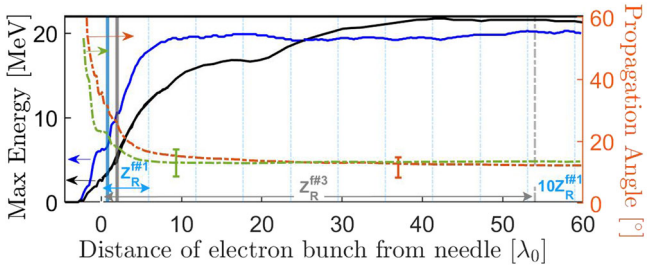

Fig. 5 | Evolution of energy and propagation direction. On the left *y*-axis we show the evolution of maximum electron energy for *f*#1 (solid blue) and *f*#3 (solid black) and on the right *y*-axis we show the expected propagation angle of highest energy electrons from the plane wave estimate (see section Simulations) for *f*#1 (green dashed) and *f*#3 (orange dashed) as a function of the distance from nanotip. The two data points are average azimuth angle from PIC simulations (error bar due to angular spread). Dashed vertical lines indicate a Rayleigh length and solid lines discriminate VLA from nanotip field acceleration.

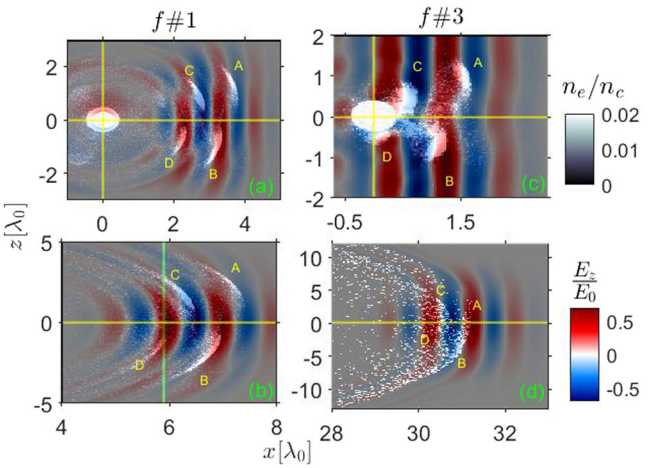

Fig. 6 | Electron—laser field dephasing. Dephasing for both f#1 (**a**, **b**) and f#3 (**c**, **d**), as seen by the location and spread of the electron bunches (electron density normalized to the critical density [$n_c = 2 \times 10^{21}\mathrm{cm}^{-3}$] in black-white) in the laser electric field (red-blue color scale). The electrons have travelled (**b**) one or (**d**) half a Rayleigh length for f#1 and f#3, respectively.

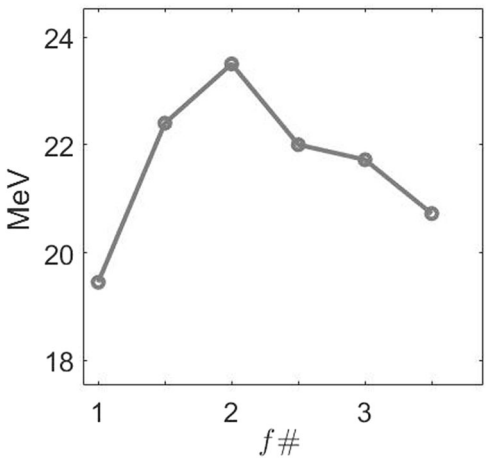

Fig. 7 | Simulated maximum energy gained by the electrons as a function of f number. Electron energies are taken at ~1.3Z_R except for *f*#3.5 where energy was taken a little earlier due to computational limitations.

Now that we have confirmed that our simulations reproduce the physics of the experiment, we discuss why the weaker electromagnetic field provided by f#3 focusing yields the same maximal electron energies. The evolution of the electron bunch energy as a function of distance from the nanotip is shown in Fig. 5. For f#1 the energy saturates at about one Rayleigh length[7,19] and does not change up to ten Rayleigh lengths, where the laser intensity is lower than the relativistic limit. Therefore, we conclude that the focal spot acceleration mechanism is relevant for our case and electrons are accelerated up to the Rayleigh range by a strong and almost constant electric field. The electron energy may be estimated according to some basic considerations. The electron energy change from the injection point (t_1 and x_1) is given by $W \approx \int_{x_1}^{Z_R} E_{acc} ds$, where $\mathbf{E}_{acc}$ is the accelerating field and ds is the length element along the trajectory. There are three main factors to consider: the strength of the accelerating field, $E_{acc} \propto E_0 \propto 1/f\#$; the longitudinal distance over which this field is sustained, $Z_R \propto (f\#)^2$; and dephasing, which controls how much of this distance actually contributes. Dephasing in VLA is reached when an electron gets out of the half-optical-cycle-long accelerating region, in contrary to laser wakefield acceleration where it is about a half plasma wavelength, i.e., about the laser pulse duration. If depahsing dominates the process, electron bunches may still be trapped and gain energy from the next optical cycle of the laser field[17]. In the absence of dephasing the energy $W \propto E_0 Z_R \propto f\#$. In other words, the weaker focusing decreases the accelerating field, but increases the acceleration length by a greater factor, such that the final electron energy gain will be higher. There is nevertheless a limit set by dephasing, i.e., when the copropagating electrons leave the accelerating half of the optical cycle.

Our results show that f#1 and f#3 focusing produce similarly energetic electrons (and moreover that the energy is not higher for f#3), which indicates the potentially important role of dephasing. Indeed Fig. 5 shows for f#3 that saturation of electron energy occurs before one Rayleigh length is reached. Dephasing may further be seen in the spatial distribution of the electron bunches, shown in Fig. 6. Whereas for f#1 the most energetic bunches (B and C) are still in the same half cycle after one Rayleigh length, for f#3 these bunches have fallen behind by $\lambda_0/4$, arriving in the following half cycle, before even a single Rayleigh length has been reached. This indicates that continuous energy gain has terminated and dephasing has set in.

Our simulations show that dephasing plays a significant role for f#3 focusing, which points towards possible optimization criteria. We estimate that in our case an optimum is reached at about f#2, where the balance between acceleration distance and accelerating field results in peak energies of 22-25 MeV (assuming no dephasing). This optimal focusing and peak electron energy was indeed confirmed with PIC simulations. This can be seen in Fig. 7 which shows the maximum energy gained by the electrons as a function of f# when the same laser is focused with different f number focusing between 1 to 3.5. There is a clear optimum focusing (f# between 1.5 to 2) below and beyond which the maximum energy begins to reduce.

Conclusion

In conclusion, we have investigated VLA experimentally and numerically, using nanotips as electron injectors in different focusing geometries. Our experimental results reveal that VLA does not necessarily benefit from tighter focusing, even though it produces stronger electromagnetic fields, and these are generally considered to be superior for laser-based acceleration schemes, and especially in nanophotonics. Instead, it is the interplay between diffraction and dephasing that is a key factor. This is shown by our comparison of f#1 and f#3 focusing, which yielded comparable total charges and electron spectra, especially peak energies. The decreased laser electric field in the latter case is more than compensated by the increased acceleration length, which we find to be limited mainly to the Rayleigh length. This paves the way towards generation of high charge, high energy, nanoscale electron bunches that could drive, e.g., an attosecond Thomson X-ray source[34].

Methods

Laser

The laser pulses in the experiment were generated with the Light Wave Synthesizer 20 system[28]. Pulses with 740 nm central wavelength, 4.8 fs full

width at half maximum (FWHM) duration, 70–80 mJ energy, and linear polarization perpendicular to the nanontip, were sent to the experimental chamber, where ≈ 40 mJ was delivered to target. Two different focusing configurations were used: f#1 and f#3. The FWHM spot sizes were 1.23 μm and 3.65 μm, respectively. These correspond to peak intensities of $I_0 = 2.4 \times 10^{20}$ W/cm^2 and 3.6×10^{19} W/cm^2, or to normalized vector potentials $a_0 = eE_0/m_e c\omega_0$ of 9.8 and 3.8, respectively. Here e is the electron charge, m_e is the electron mass, E_0 is the laser electric field strength, ω_0 the central laser frequency and c the velocity of light in vacuum. The estimated Rayleigh length (Z_R) is 4.6 μm with f#1 and 40 μm with f#3.

Target alignment

For each laser shot (whether f#1 or f#3), a new tungsten nanotip (apex diameter ≤100 nm)[37–39] was positioned with sub-μm accuracy in the focus, while the laser intensity was reduced to $<10^{12}$ W/cm^2 (which was the measured damage threshold) to avoid premature damage to the tip. After the alignment, a single laser pulse at full power was released.

Target alignment stability

The standard deviation (STD) in pointing stability of the laser in the experiment is better than $5 \cdot 10^{-6}$ rad, i.e., better than 20% of the FWHM of the focus. Additionally, the spatial accuracy for aligning the tips into the focus (for f#1) is of the order of 50% of the focus FWHM for the x and z direction (horizontal and longitudinal), and in the order of the focus size for the y direction (vertical). We consider that these fluctuations, especially the alignment, are the cause of the observed variation in electron direction (especially in the polar angle). The electron direction fluctuations (STD) for f#1 were 4.8° and 1.8° for the polar and azimuth angle, respectively. For f#3 these were 1.5° and 1.7° in the polar and azimuth angle, respectively.

Electron beam characterization

The accelerated electrons were characterized by measuring their total charge and their angular distribution with an absolutely calibrated scintillating screen of approximately 100 μm thickness (Lanex Biomax MS, Kodak)[40,41], as schematically shown in Fig. 1b, c. A thin aluminum foil (10 μm, Goodfellow) was placed immediately before the scintillating screen to filter out the laser light. Furthermore, a 1 mm thick lead shield was placed before the screen in some shots to filter out low-energy electrons (<2.5 MeV completely and <4 MeV low transmission). The angle-resolved energy spectrum was also measured, using a dipole spectrometer with a scintillating screen and a complementary metal-oxide-semiconductor (CMOS) detector[42]. The electron spectrometer could be rotated around the azimuth angle and had an acceptance half-angle of 7.6° and 5.5° for the f#1 and f#3 focusing configurations, respectively.

PIC simulations

The simulations were performed using Smilei-v4.7[35] in full 3D using a moving window technique that follows the accelerated electrons. The two focusing geometries were modelled by a p-polarised (perpendicular to the tip) laser pulse Gaussian in time with FWHM duration of 4.5 fs and a central wavelength of $\lambda_0 = 0.74$ μm, and spatial Gaussian beam with a focal spot size (FWHM) of 1.2 μm or 3.6 μm (amplitude $a_0 = 9.5$ or $a_0 = 3.7$, Rayleigh length $Z_R = 4.4$ μm or 40 μm) for f#1 or f#3, respectively.

In the focus, the tip of a tungsten nano-needle plasma was placed. The structure of the tungsten needle is a superposition of a conical frustum and a hemisphere with the radius of the hemisphere being equal to the top radius of the frustum. The top and bottom radii of the conical frustum are 96 nm and 0.61 μm, respectively, and the height is 4 μm. For the *f*#3 configuration, this needle structure is extended by 3.7 μm in the direction of the base of the cone in order to include the larger focal spot area. The tungsten plasma with an electron density of $100n_c$, ion charge state of 44, and plasma temperature of 5 keV is initialised, where n_c is the classical critical density ($n_c = m_e\omega_0^2/4\pi e^2 = 2 \times 10^{21}$ cm^{-3}). Here e is the electron charge, m_e is the electron mass, and ω_0 the central laser frequency. The ion charge-to-mass ratio is $44e/184m_p$, where m_p is the proton mass.

The simulation box is a moving window, with a cell size of 11.5 nm with 64 particles in each cell, which follows the electron bunches moving along with the laser pulse for multiple Rayleigh lengths ($5.9\lambda_0$ for *f*#1 and $54\lambda_0$ for *f*#3).

Data availability

The data underlying the results presented in this paper are not publicly available at this time but may be obtained from the authors upon reasonable request.

Code availability

The code used for the simulations and data analysis is available from the corresponding authors upon reasonable request.

Received: 8 March 2024; Accepted: 16 August 2024;
Published online: 02 September 2024

References

1. Humphries, S. *Principles of charged particle acceleration* (Courier Corporation, 2013).
2. Peralta, E. A. et al. Demonstration of electron acceleration in a laser-driven dielectric microstructure. *Nature* **503**, 91–94 (2013).
3. Gahn, C. et al. Multi-mev electron beam generation by direct laser acceleration in high-density plasma channels. *Phys. Rev. Lett.* **83**, 4772 (1999).
4. Esarey, E., Schroeder, C. B. & Leemans, W. P. Physics of laser-driven plasma-based electron accelerators. *Rev. Mod. Phys.* **81**, 1229–1285 (2009).
5. Wang, P. et al. Vacuum electron acceleration by an intense laser. *Appl. Phys. Lett.* **78**, 2253–2255 (2001).
6. Pang, J. et al. Subluminous phase velocity of a focused laser beam and vacuum laser acceleration. *Phys. Rev. E* **66**, 066501 (2002).
7. Popov, K., Bychenkov, V. Y., Rozmus, W. & Sydora, R. Electron vacuum acceleration by a tightly focused laser pulse. *Phys. Plasmas* **15**, 013108 (2008).
8. Esarey, E., Sprangle, P. & Krall, J. Laser acceleration of electrons in vacuum. *Phys. Rev. E* **52**, 5443–5453 (1995).
9. Hartemann, F. V. et al. Nonlinear ponderomotive scattering of relativistic electrons by an intense laser field at focus. *Phys. Rev. E* **51**, 4833–4843 (1995).
10. Cheng, Y. & Xu, Z. Vacuum laser acceleration by an ultrashort, high-intensity laser pulse with a sharp rising edge. *Appl. Phys. Lett.* **74**, 2116–2118 (1999).
11. Salamin, Y. I. & Keitel, C. H. Electron acceleration by a tightly focused laser beam. *Phys. Rev. Lett.* **88**, 095005 (2002).
12. Hu, S. X. & Starace, A. F. Gev electrons from ultraintense laser interaction with highly charged ions. *Phys. Rev. Lett.* **88**, 245003 (2002).
13. Ramsey, D., Franke, P., Simpson, T. T., Froula, D. H. & Palastro, J. P. Vacuum acceleration of electrons in a dynamic laser pulse. *Phys. Rev. E* **102**, 043207 (2020).
14. Plettner, T. et al. Visible-laser acceleration of relativistic electrons in a semi-infinite vacuum. *Phys. Rev. Lett.* **95**, 134801 (2005).
15. Cline, D. et al. First observation of acceleration of electrons by a laser in a vacuum. *J. Mod. Phys.* **4**, 1–6 (2013).
16. Braenzel, J. et al. Amplification of relativistic electron bunches by acceleration in laser fields. *Phys. Rev. Lett.* **118**, 014801 (2017).
17. Elkind, M. et al. Intense laser interaction with micro-bars. *Sci. Rep.* **13**, 21345 (2023).
18. Thévenet, M. et al. Vacuum laser acceleration of relativistic electrons using plasma mirror injectors. *Nat. Phys.* **12**, 355–360 (2016).
19. Cardenas, D. E. et al. Sub-cycle dynamics in relativistic nanoplasma acceleration. *Sci. Rep.* **9**, 7321 (2019).
20. Singh, P. K. et al. Vacuum laser acceleration of super-ponderomotive electrons using relativistic transparency injection. *Nat. Commun.* **13**, 54 (2022).

21. Malka, G., Lefebvre, E. & Miquel, J. L. Experimental observation of electrons accelerated in vacuum to relativistic energies by a high-intensity laser. *Phys. Rev. Lett.* **78**, 3314–3317 (1997).
22. Mora, P. & Quesnel, B. Comment on "experimental observation of electrons accelerated in vacuum to relativistic energies by a high-intensity laser". *Phys. Rev. Lett.* **80**, 1351 (1998).
23. McDonald, K. T. Comment on "experimental observation of electrons accelerated in vacuum to relativistic energies by a high-intensity laser". *Phys. Rev. Lett.* **80**, 1350 (1998).
24. Varin, C. & Piché, M. Relativistic attosecond electron pulses from a free-space laser-acceleration scheme. *Phys. Rev. E* **74**, 045602(R) (2006).
25. Wong, L. J. et al. Laser-induced linear-field particle acceleration in free space. *Sci. Rep.* **7**, 11159 (2017).
26. Payeur, S. et al. Generation of a beam of fast electrons by tightly focusing a radially polarized ultrashort laser pulse. *Appl. Phys. Lett.* **101**, 041105 (2012).
27. Carbajo, S. et al. Direct longitudinal laser acceleration of electrons in free space. *Phys. Rev. Accelerators Beams* **19**, 021303 (2016).
28. Rivas, D. E. et al. Next generation driver for attosecond and laser-plasma physics. *Sci. Rep.* **7**, 5224 (2017).
29. Popov, K., Bychenkov, V. Y., Rozmus, W., Sydora, R. & Bulanov, S. Vacuum electron acceleration by tightly focused laser pulses with nanoscale targets. *Phys. Plasmas* **16**, 053106 (2009).
30. Liseykina, T., Pirner, S. & Bauer, D. Relativistic attosecond electron bunches from laser-illuminated droplets. *Phys. Rev. Lett.* **104**, 095002 (2010).
31. Andreev, A. & Platonov, K. Y. Generation of electron nanobunches and short-wavelength radiation upon reflection of a relativistic-intensity laser pulse from a finite-size target. *Opt. Spectrosc.* **114**, 788–797 (2013).
32. Naumova, N. et al. Attosecond electron bunches. *Phys. Rev. Lett.* **93**, 195003 (2004).
33. Di Lucchio, L. & Gibbon, P. Relativistic attosecond electron bunch emission from few-cycle laser irradiated nanoscale droplets. *Phys. Rev. ST Accel. Beams* **18**, 023402 (2015).
34. Horný, V. & Veisz, L. Generation of single attosecond relativistic electron bunch from intense laser interaction with a nanosphere. *Plasma Phys. Controlled Fusion* **63**, 125025 (2021).
35. Derouillat, J. et al. Smilei : A collaborative, open-source, multi-purpose particle-in-cell code for plasma simulation. *Computer Phys. Commun.* **222**, 351–373 (2018).
36. Gibbon, P. *Short Pulse Laser Interactions with Matter* (Imperial College Press, London, 2005), 1st edn.
37. Lucier, A.-S. *Preparation and characterization of Tungsten tips suitable for molecular electronics studies*. Master thesis, (McGill University, 2004).
38. Hobara, R., Yoshimoto, S., Hasegawa, S. & Sakamoto, K. Dynamic electrochemical-etching technique for tungsten tips suitable for multi-tip scanning tunneling microscopes. *e-J. Surf. Sci. Nanotechnol.* **5**, 94–98 (2007).
39. Toh, S., Tan, H., Lam, J., Hsia, L. & Mai, Z. Optimization of ac electrochemical etching for fabricating tungsten nanotips with controlled tip profile. *J. Electrochem. Soc.* **157**, E6 (2009).
40. Buck, A. et al. Absolute charge calibration of scintillating screens for relativistic electron detection. *Rev. Sci. Instrum.* **81**, 033301 (2010).
41. Kurz, T. et al. Calibration and cross-laboratory implementation of scintillating screens for electron bunch charge determination. *Rev. Sci. Instrum.* **89**, 093303 (2018).
42. Holgerson, A. *Detection of relativistic electron bunches driven by few-cycle laser pulses*. Master thesis, Umeå University http://urn.kb.se/resolve?urn=urn:nbn:se:umu:diva-167797 (2020).

Acknowledgements

A.D.A. and S.B. contributed equally to this work. The authors thank Roushdey Salh for the technical support. L.V., D.H., A.G. and M.M. acknowledge the support from Vetenskapsrådet (2019-02376). L.V. acknowledges the support from Vetenskapsrådet (2020-05111), Knut och Alice Wallenbergs Stiftelse (2019.0140), and Kempestiftelserna (SMK21-0017). S.B. and A.G. acknowledge the computational resources provided by the National Academic Infrastructure for Super Computing in Sweden (NAISS-2023/5-43) and (NAISS 2023/22-8).

Author contributions

Conceptualization and methodology: L.V., and A.D.A.; Experimental realization: A.D.A, A.M., and J.T.M.; Simulations: S.B.; Nano-needle production: A.D.A. and H.R.B; data analysis: A.D.A., S.B., and L.V.; Discussion and interpretation: A.D.A, S.B., J.T.M., A.M., P.F., T.B., A.G., D.H., M.M., and L.V; visualization: S.B., A.D.A., and L.V; Manuscript writing and editing: A.D.A, S.B., J.T.M., A.M., P.F., H.R.B, T.B., A.G., D.H., M.M., and L.V; Project supervision: L.V., A.G., M.M., and D.H.

Funding

Open access funding provided by Umea University.

Competing interests

The authors declare no competing interests.

Additional information

Supplementary information The online version contains supplementary material available at https://doi.org/10.1038/s42005-024-01781-9.

Correspondence and requests for materials should be addressed to Aitor De Andres, Shikha Bhadoria or Laszlo Veisz.

Peer review information *Communications Physics* thanks Ishay Pomerantz, Alessandro Maffini and the other, anonymous, reviewer(s) for their contribution to the peer review of this work.

Reprints and permissions information is available at http://www.nature.com/reprints

Publisher's note Springer Nature remains neutral with regard to jurisdictional claims in published maps and institutional affiliations.

Open Access This article is licensed under a Creative Commons Attribution 4.0 International License, which permits use, sharing, adaptation, distribution and reproduction in any medium or format, as long as you give appropriate credit to the original author(s) and the source, provide a link to the Creative Commons licence, and indicate if changes were made. The images or other third party material in this article are included in the article's Creative Commons licence, unless indicated otherwise in a credit line to the material. If material is not included in the article's Creative Commons licence and your intended use is not permitted by statutory regulation or exceeds the permitted use, you will need to obtain permission directly from the copyright holder. To view a copy of this licence, visit http://creativecommons.org/licenses/by/4.0/.

© The Author(s) 2024